RESEARCH ARTICLE
SOLID EARTH: SEISMOLOGY

Earth and Planetary Physics
3: 253–267, 2019
doi: 10.26464/epp2019027

Geometry and tectonic deformation of the seismogenic structure for the 8 August 2017 M_S 7.0 Jiuzhaigou earthquake sequence, northern Sichuan, China

Feng Long[1], GuiXi Yi[1,2*], SiWei Wang[1], YuPing Qi[1], and Min Zhao[1]

[1]Sichuan Earthquake Agency, Chengdu 610041, China;

[2]Sichuan Seistech Corporation Ltd., Chengdu 610041, China

Abstract: To reveal the geometry of the seismogenic structure of the Aug. 8, 2017 M_S 7.0 Jiuzhaigou earthquake in northern Sichuan, data from the regional seismic network from the time of the main event to Oct. 31, 2017 were used to relocate the earthquake sequence by the tomoDD program, and the focal mechanism solutions and centroid depths of the $M_L \geq 3.5$ events in the sequence were determined using the CAP waveform inversion method. Further, the segmental tectonic deformation characteristics of the seismogenic faults were analyzed preliminarily by using strain rosettes and areal strains (*As*). The results indicate: (1) The relocated M_S 7.0 Jiuzhaigou earthquake sequence displays a narrow ~ 38 km long NNW-SSE-trending zone between the NW-striking Tazang Fault and the nearly NS-striking Minjiang Fault, two branches of the East Kunlun Fault Zone. The spatial distribution of the sequence is narrow and deep for the southern segment, and relatively wide and shallow for the northern segment. The initial rupture depth of the mainshock is 12.5 km, the dominant depth range of the aftershock sequence is between 0 and 10 km with an average depth of 6.7 km. The mainshock epicenter is located in the middle of the aftershock region, showing a bilateral rupture behavior. The centroid depths of 32 $M_L \geq 3.5$ events range from 3 to 12 km with a mean of about 7.3 km, consistent with the predominant focal depth of the whole sequence. (2) The geometric structure of the seismogenic fault on the southern section of the aftershock area (south of the mainshock) is relatively simple, with overall strike of ~150° and dip angle ~75°, but the dip angle and dip-orientation exhibit some variation along the segment. The seismogenic structure on the northern segment is more complicated; several faults, including the Minjiang Fault, may be responsible for the aftershock activities. The overall strike of this section is ~159° and dip angle is ~59°, illustrating a certain clockwise rotation and a smaller dip angle than the southern segment. The differences between the two segments demonstrate variation of the geometric structure along the seismogenic faults. (3) The focal mechanism solutions of 32 $M_L \geq 3.5$ events in the earthquake sequence have obvious segmental characteristics. Strike-slip earthquakes are dominant on the southern segment, while 50% of events on the northern segment are thrusting and oblique thrusting earthquakes, revealing significant differences in the kinematic features of the seismogenic faults between the two segments. (4) The strain rosettes for the mainshock and the entire sequence of 31 $M_L \geq 3.5$ aftershocks correspond to strike-slip type with NWW-SEE compressional white lobes and NNE-SSW extensional black lobes of nearly similar size. The strain rosette and *As* value of the entire sequence of 22 $M_L \geq 3.5$ events on the southern segment are the same as those of the M_S 7.0 mainshock, indicating that the tectonic deformation here is strike-slip. However, the strain rosette of the entire sequence of 10 $M_L \geq 3.5$ events on the northern segment show prominent white compressional lobes and small black extensional lobes, and the related *As* value is up to 0.52, indicating that the tectonic deformation of this segment is oblique thrusting with a certain strike-slip component. Differences between the two segments all reveal distinctly obvious segmental characteristics of the tectonic deformation of the seismogenic faults for the Jiuzhaigou earthquake sequence.

Keywords: M_S 7.0 Jiuzhaigou earthquake sequence; relocation; focal mechanism; seismogenic structure geometry; tectonic deformation

Citation: Long, F., Yi, G. X., Wang, S. W., Qi, Y. P., and Zhao, M. (2019). Geometry and tectonic deformation of the seismogenic structure for the 8 August 2017 M_S 7.0 Jiuzhaigou earthquake sequence, northern Sichuan, China. *Earth Planet. Phys.*, *3*(3), 253–267. http://doi.org/10.26464/epp2019027

1. Introduction

At Beijing time 21h19m of Aug. 8, 2017, a strong earthquake of M_S 7.0 occurred in the Jiuzhaigou County of Aba Prefecture, Sichuan Province, China, in the northern part of the Bayan Har block at the east margin of the Tibetan Plateau; its epicenter (33.22°N, 103.83°E) was located in the area bounded by the NW-trending Tazang Fault and near-NS-trending Minjiang Fault (two branch faults of the East Kunlun Fault Zone) and the near-EW-trending Xueshanliangzi Fault on the south (Figure 1). Based on seismic damage investigation, strong motion record analysis, and aerial remote sensing image interpretation of seismic damage, the

Correspondence to: G. X. Yi, yigx64@163.com
Received 29 JAN 2019; Accepted 12 APR 2019.
Accepted article online 30 APR 0219.

China Earthquake Administration determined that the isoseismal maps of the M_S 7.0 Jiuzhaigou earthquake are approximately ellipses with NNW-trending major axes, the meizoseismic zone (intensity IX) has an area of 139 km^2, and the area of intensity VIII is 778 km^2 (http://www.cea.gov.cn/cea/dzpd/dzzt/369861/369862/3583320/index.html, see the shaded red ellipse in Figure 1).

After the occurrence of the M_S 7.0 Jiuzhaigou earthquake, a number of research groups studied its source parameters, seismogenic structures, rupture characteristics, and source environment based on the data of seismic phases and waveforms recorded by regional seismic station networks, remote seismic waveforms, strong motion observations, GNSS, and InSAR (Shan XJ et al., 2017; Fang LH et al., 2018; Li MJ et al., 2018; Liang JH et al., 2018; Liang SS et al., 2018; Wen XZ, 2018; Xu LS et al., 2018; Yang Y and Chang LJ, 2018; Zhao B et al., 2018a, b); abundant results have been achieved. In spite of controversy over the specific seismogenic structure, a consensus has gradually been reached that the seismogenic fault of the mainshock should be one of the splayed branch faults at the east end of the East Kunlun Fault Belt (Xu XW et al., 2017; Yi GX et al., 2017a; Han LB et al., 2018; Lu RQ et al., 2018; Qi YP et al., 2018; Sun JB et al., 2018; Xie ZJ et al., 2018). However, it should be pointed out that different research groups have reported significantly different mainshock focal depths of the M_S 7.0 Jiuzhaigou earthquake (Table 1); in addition, because most of the earthquake location studies have used only the early sequence data, the resultant spatial distribution characteristics of the aftershock sequence also differ significantly, leading to obviously different, even contradictory, understandings of the geometrical characteristics of the seismogenic structure of this earthquake sequence.

In this paper, on the basis of an earlier work (Yi GX et al., 2017a), we use seismic data recorded by regional seismic networks up to Oct. 10, 2017, fully two months after the main event, and employ the tomoDD method developed by Zhang HJ and Thurber(2003, 2006) to relocate the M_S 7.0 Jiuzhaigou earthquake sequence. Compared to the conventional double difference method (Waldhauser and Ellsworth, 2000), tomoDD allows carrying out a simultaneous inversion for the 3D velocity model and source locations; the simultaneous use of the constraints of absolute and relative arrival times leads to higher accuracies of absolute and relative source locations. In addition, we use the CAP waveform inversion method (Zhao LS and Helmberger, 1994; Zhu LP and Helmberger, 1996) to determine the focal mechanism solutions of $M_L \geq 3.5$ earthquakes in this sequence. This method divides the waveform into body and surface waves for sliding fitting, which makes the result insensitive to the velocity model (Zheng Y et al., 2009); besides, the depth phases and surface wave amplitude also put effective constraints on the focal depths (Luo Y et al., 2015). Finally we use the strain rosette method of Amelung and King (1997) and the areal strain *As* of Vallage et al. (2014) to analyze the geometric,

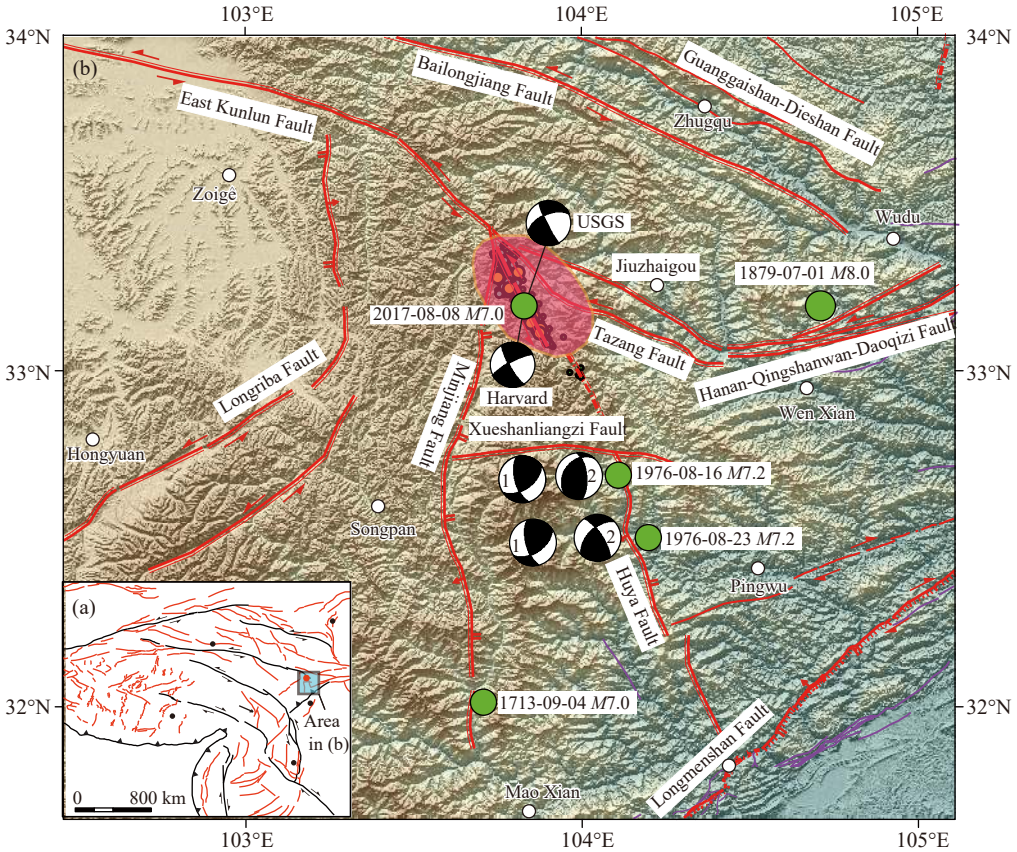

Figure 1. Regional tectonic settings and the historical $M_S \geq 7.0$ earthquakes since 1700 around the epicenter of the M_S 7.0 Jiuzhaigou event. The blue shadow box in the inset indicates the location of Figure 1. The green circles mark the epicenters of historical $M_S \geq 7.0$ earthquakes, and the shaded red ellipse indicates the intensity VIII area of the M_S 7.0 Jiuzhaigou earthquake. The focal mechanism solutions of the two M_S 7.2 Songpan-Pingwu earthquakes in 1976 come from Jones et al. (1984) and Kan R J et al. (1983), marked by Numbers 1 and 2, respectively.

Table 1. The depths of the M_S 7.0 Jiuzhaigou mainshock, depth range of aftershocks, long-axis of the aftershock area, and the depth range of the main rupture derived by different organizations and teams

Source	Magnitude M_w	Initial rupture depth (km)	Centroid depth (km)	Aftershock depths (km)	Aftershock zone length (km)	Dominant rupture depths (km)	Seismogenic structure
CENC	–	20	–	–	–	–	–
USGS	6.5	9	13.5	–	–	–	–
HRV	6.5	–	14.9	–	–	–	–
GFZ	6.5	9	10	–	–	–	–
Ji LY et al. (2017)	6.46	–	–	–	–	4–16	Shuzheng Fault
Shan B et al. (2017)	6.5	–	6	5–20	–	5–12	–
Shan XJ et al. (2017)	6.5	–	–	–	–	1–15	Northern extension branch of Huya Fault
Sun JB et al. (2018)	>6.3	–	–	–	–	5–12	Northern extension of Huya Fault
Yi GX et al. (2017a)	6.4	16.9	5	6–12	38	–	A branch of East Kunlun Fault Shuzheng Fault
Zhang X et al. (2017)	6.5	–	11	5–15	–	–	–
Zheng XJ et al. (2017)	6.5	–	–	–	–	0–10	–
An YR et al. (2018)	6.5	20	11	5–20	>30	–	Huya Fault
Chen W et al. (2018)	6.5	10.86	–	–	–	5–20	Northern section of Huya Fault
Fang LH et al. (2018)	–	20.4	≥14.3	4–20	42	–	Northern section of Huya Fault
Han LB et al. (2018)	6.5	21	14	3–20	34	–	Branch of East Kunlun Fault
Liang JH et al. (2018)	–	16	–	5–15	35	–	Northwestern section of Huya Fault
Liang SS et al. (2018)	6.5	23	15.5	4–22	58	–	Branch of southern section of Tazang Fault and northern section of Huya Fault
Wang YB et al. (2018)	6.4	–	–	–	–	~7	–
Xie ZJ et al. (2018)	6.5	20	6	5–20	33	3–13	Branch of East Kunlun Fault Belt
Xu LS et al. (2018)	–	15.8	–	–	–	–	–
Zhao B et al.(2018a, b)	–	–	8.2–9.0	–	–	–	Shuzheng Fault
Zhao DZ et al. (2018)	6.5	–	–	–	–	2–15	–

kinematic, and tectonic deformation characteristics of the seismogenic fault of the Jiuzhaigou earthquake sequence.

2. Earthquake Sequence Relocation and Seismogenic Fault Geometry Analysis

From Aug. 8 to Oct. 31, 2017, the Sichuan Seismic Network recorded altogether 8667 aftershocks above M_L 0 of this earthquake sequence (including 2308 single station recorded events). Among them there are 3976 events of M_L 0.0–0.9, 3929 of M_L 1.0–1.9, 667 of M_L 2.0–2.9, 80 of M_L 3.0–3.9, and 15 of M_L 4.0–4.9 (4 above M_S 4.0). The largest aftershock is the M_S 4.8 event at 10h17m of Aug. 9. The sequence contains mainly small earthquakes of $M_L \leq 2.0$.

Accurate location of an earthquake sequence is the basis for de-

termining the geometry of its seismogenic fault (Rubin, 2002; Yi GX et al., 2015). In order to improve the location accuracy of the Jiuzhaigou earthquake sequence, we utilize the seismic phase report of Sichuan Seismological Station Network Center, take the one-dimensional velocity model of Yi GX et al. (2017a) for Jiuzhaigou area as the initial model (Figure 2), and use the tomoDD method (Zhang HJ and Thurber, 2003, 2006) to relocate events of this sequence that were recorded by more than 4 stations. The stations used in the relocation include all permanent stations within 300 km from the epicenter and 6 portable stations deployed after the mainshock (see Figure 2 for station distribution); the geographic coordinates and data starting times of the 6 portable stations are listed in Table 2.

Using the tomoDD method we relocated 2842 $M_L \geq 1.0$ earthquakes in the Jiuzhaigou sequence from Aug. 8 to Oct. 31, 2017. The relative location error is 0.32 km and 0.52 km respectively in the horizontal and vertical directions, while the travel time residual is 0.08 s. The source parameters of the M_S 7.0 mainshock after relocation are as follows: occurrence time 2017-08-08 21:19:47.4, epicenter location 103.816°E, 33.204°N, and focal depth 12.5 km. The relocated source parameters of the largest aftershock in the se-

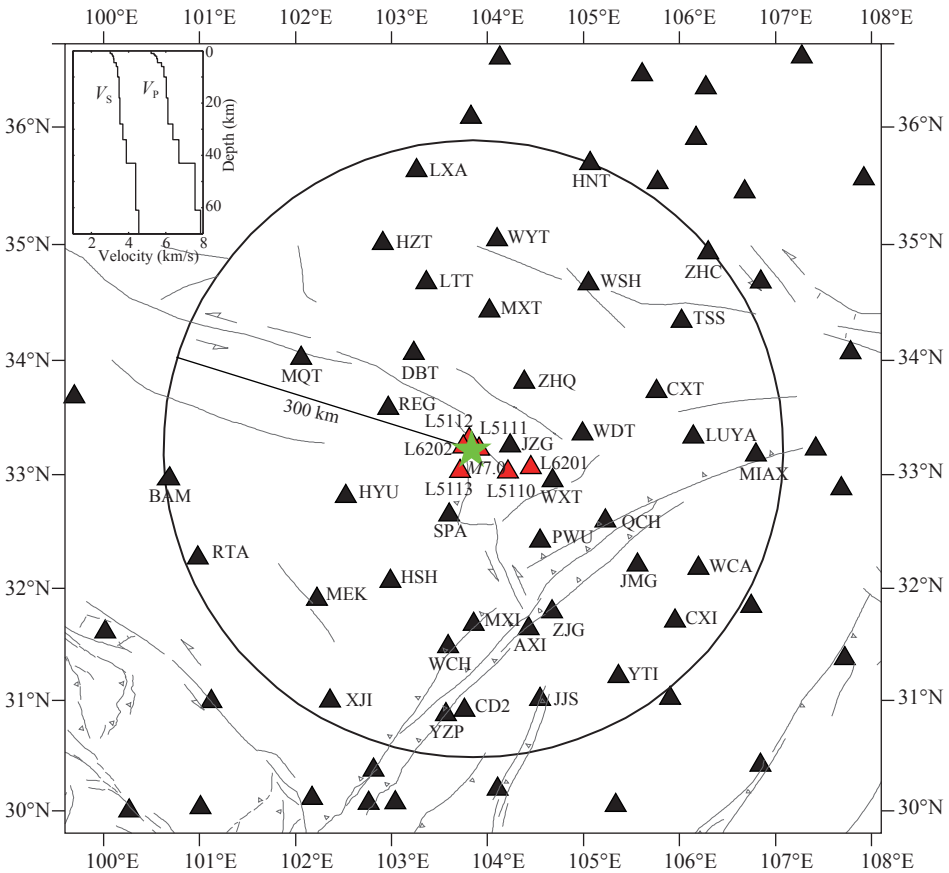

Figure 2. Distribution of seismic stations for relocation and focal mechanism calculation of the M_S 7.0 Jiuzhaigou earthquake sequence. The green star marks the M_S 7.0 Jiuzhaigou mainshock. The black and red triangles represent permanent and portable seismic stations, respectively. Black circle indicates the range within epicentral distance of 300 km. 1-D velocity model of the Jiuzhaigou area from Yi GX et al. (2017a) is showed on the left top corner.

Table 2. The locations and data starting times of the six portable stations

Number	Name	Station location			Data starting time	Distance to the epicenter of the mainshock (km)
		Longitude (°E)	Latitude (°N)	Elevation (km)	year-month-day hour:min	
1	L6201	104.448	33.0646	1.142	2017-08-09 18:31	60.9
2	L5110	104.207	33.032	1.800	2017-08-09 19:03	41.1
3	L5111	103.910	33.228	2.190	2017-08-10 13:50	9.1
4	L5112	103.8075	33.3099	2.204	2017-08-10 16:25	11.8
5	L5113	103.712	33.0323	3.495	2017-08-11 16:30	21.3
6	L6202	103.746	33.2461	2.653	2017-08-12 07:50	8.0

quence (M_S 4.8, Aug. 9, 2017) are as follows: occurrence time 2017-08-09 10:17:03.5, epicenter location 103.833°E, 33.155°N, and focal depth 10.6 km.

Figure 3 shows the focal depth histograms before and after relocation; the red and blue/green colors represent the aftershock frequencies in the first three days and thereafter, respectively. It can be seen that before relocation the dominant focal depth range is 4–18 km (Figure 3a) with an average depth of 10.7 km; after relocation the average focal depth is reduced to 6.7 km and the dominant depth range is 0–10 km (Figure 3b). This result agrees with the main rupture depth ranges derived from different data, such as InSAR and strong motion records (Shan XJ et al., 2017; Sun JB et al., 2017; Zheng XJ et al., 2017; Xie ZJ et al., 2018; Zhao DZ et al., 2018) (Table 1). The result also shows that the depth distribution of aftershocks after three days is more concentrated (Figure 3).

The relocated Jiuzhaigou earthquake sequence is located in between the NW-trending Tazang Fault and the near-NS-trending Minjiang Fault (Figure 4); the overall shape of the dense aftershock region is a narrow zone extending in the NNW-SSE direction, its northern end deviating slightly to the north (Yi GX et al., 2017a); the strike of the major axis of the aftershock zone is basically consistent with the NNW-trending major axis of the isoseismal map (Figure 1). The M_S 7.0 mainshock is located approximately at the center of the aftershock zone; taking the mainshock as a boundary, the aftershock zone is narrow in the south and wide in the north (Yi GX et al., 2017a; Fang LH et al., 2018), and the dense aftershocks zone did not extend southward to the NNW-trending Huya Fault. It can be seen that the distribution scope of later aftershocks (green circles in Figure 4) basically accords with that of the aftershocks in the first three days (red circles in Figure 4).

The vertical profile AA' along the major axis of the aftershock zone (Figure 5) indicates that the aftershock zone is about 38 km long. There is an area of sparse aftershocks about 4 km long in the northwestern vicinity of the mainshock (marked by a black dashed-line box in Figure 5) (Han LB et al., 2018; Fang LH et al., 2018; Liang JH et al., 2018; Xie ZJ et al., 2018). This characteristic of aftershock distribution is similar to that of the M_w 6.6 earthquake of Oct. 23, 2004, in Mid-Niigata Prefecture, Japan (Kato et al., 2010) and the M_S 6.3 Kangding, Sichuan, earthquake of Nov. 22, 2014 (Yi GX et al., 2015). This sparse aftershock area may be a relatively large asperity (Aki, 1984; Zhang X et al., 2017) where the energy was fully released during the mainshock. Taking the mainshock as the boundary and dividing the aftershock zone into a southern and a northern section, it can be seen that the aftershock depth is generally deeper in the south and shallower in the north (Fang LH et al., 2018).

In order to reveal the geometrical characteristics of the seismogenic fault of this earthquake sequence, we plotted 6 vertical sections perpendicular to the long axis of the aftershock zone from south to north (Figure 6); the projection width is 2 km on each side. Section BB' is at the southern end of the aftershock zone and shows that in the first three days aftershocks are rare; thereafter the aftershock depth range here is slightly greater than that in the other 5 sections to its north. This aftershock depth distribution indicates that the fault plane here is nearly vertical in the shallow part, inclining slightly to the NE below 4 km. The CC' section shows that the aftershocks are concentrated primarily in the depth range 3–10 km, the aftershock distribution clearly displaying the character of a steep fault dipping to the SW, its dip angle estimated roughly to be about 74°. Section DD' indicates that the dominant aftershock depth is the same as in section CC'; compared to sections BB' and CC', the aftershocks are more scattered; however, the fault plane can still be seen to dip toward the SW. Section EE' passes through the epicenter of the M_S 7.0 Jiuzhaigou mainshock, where the aftershocks are concentrated above depth 10 km; its aftershock distribution shows that the fault structure here is simple, with a nearly upright fault plane. Different from the simple fault structures in the 4 sections BB'–EE' to the south of the mainshock, aftershocks in the section FF' to the north of the mainshock are mainly above the depth 8 km and the depth range is slightly smaller than those in the southern sections; from the aftershock distribution it can be seen that the fault plane below 3 km is here roughly vertical, but above 3 km the fault structure is relatively complex; besides an upright fault plane there is also a SW-dipping fault plane. Aftershocks in the section GG' at the northern end are relatively shallow, occurring mainly above depth 6 km, and are more spread, implying that a number of faults were involved in these aftershock activities; this indicates that the seismogenic fault structure in this section is complicated. In fact, ac-

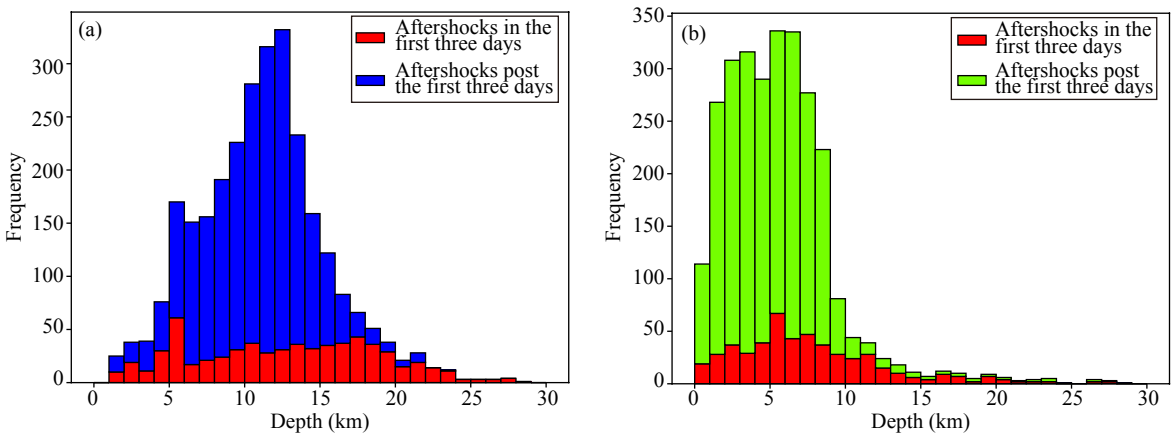

Figure 3. Histogram plots of focal depths for the M_S 7.0 Jiuzhaigou earthquake sequence before (a) and after (b) relocation.

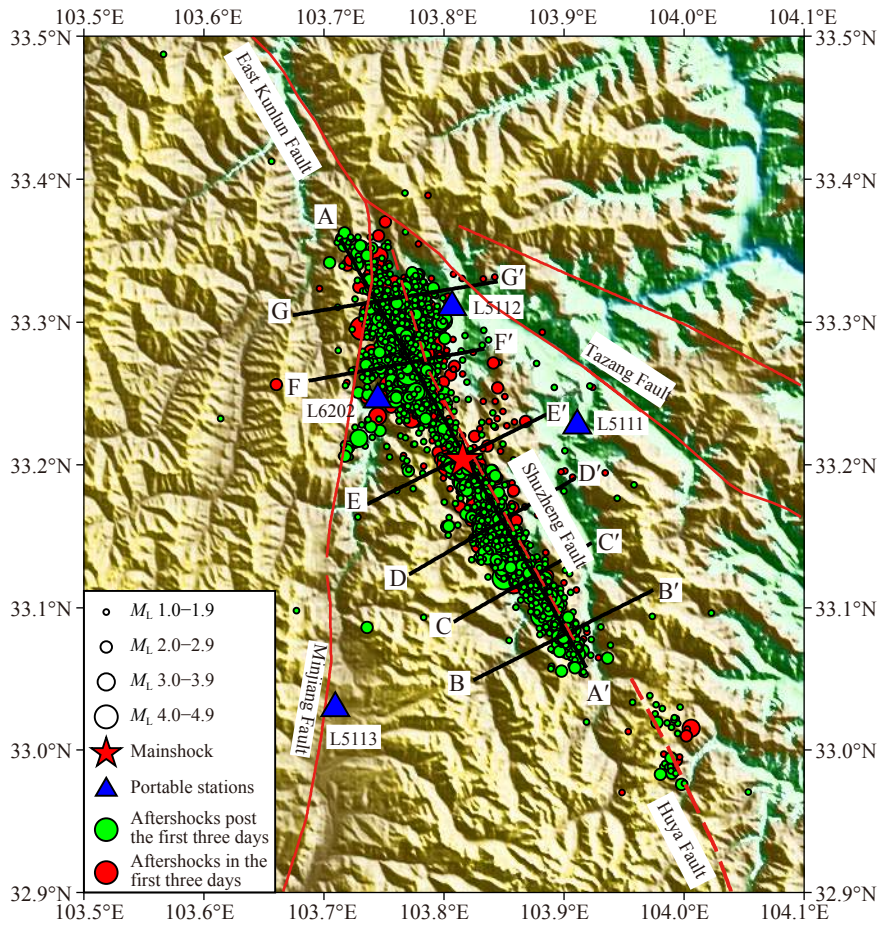

Figure 4. Map view of the relocated Jiuzhaigou earthquake sequence by Oct. 31, 2017. The red and green circles are relocated epicenters of the first 3 days and later aftershocks, respectively. The red star marks the M_S 7.0 Jiuzhaigou mainshock, and the blue triangles represent portable stations.

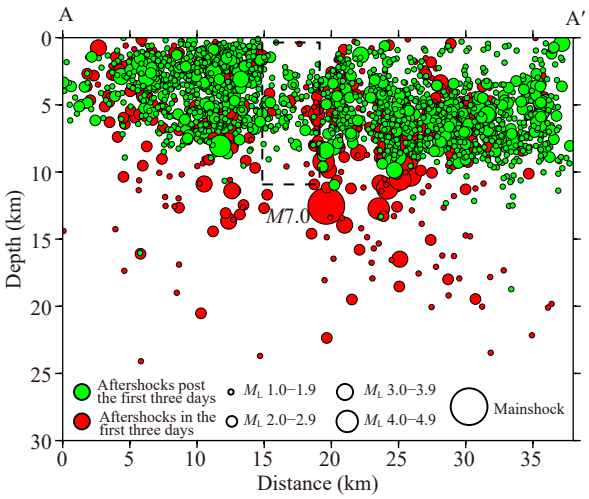

Figure 5. Vertical cross-section AA' along the strike of the long-axis of the aftershock area. The black dashed box marks the region of sparse aftershocks.

cording to the aftershock distribution in Figure 4, it can be seen that at least the northern segment of the Minjiang Fault was involved in the aftershock activity (An YR et al., 2018; Sun JB et al., 2018).

The above results indicate that while the seismogenic fault structure in the southern part of the aftershock zone is relatively simple, in the northern part it is more complicated; there may be multiple faults involved. However, even the southern segment of the seismogenic structure is not a straight fault: the fault plane is steep, but the dip angle and dip orientation still vary to some extent in different locations (Fang LH et al., 2018). These results reveal the complexity of the seismogenic fault geometry of this M_S 7.0 Jiuzhaigou earthquake sequence (Zhang X et al., 2017).

In addition, it is easy to observe from Figure 5 and Figure 6 that all 7 vertical sections show that the aftershocks after three days are concentrated at depths above 10 km, with a range of depths obviously smaller than that of the early (first three days) aftershocks. We suggest that the reason for such a difference is closely related to the lack of near-station constraints for the early events in the sequence. Previous research has established that focal depth can be effectively constrained only when station-epicenter distances are less than 1.4 times the focal depth, and S wave arrival times are accurate (Gomberg et al., 1990; Fang LH et al., 2018). Before the deployment of portable stations, the station nearest to the mainshock of the Jiuzhaigou earthquake sequence was JZG station with an epicentral distance about 40 km (Figure 2). After the mainshock, portable stations were progressively installed to im-

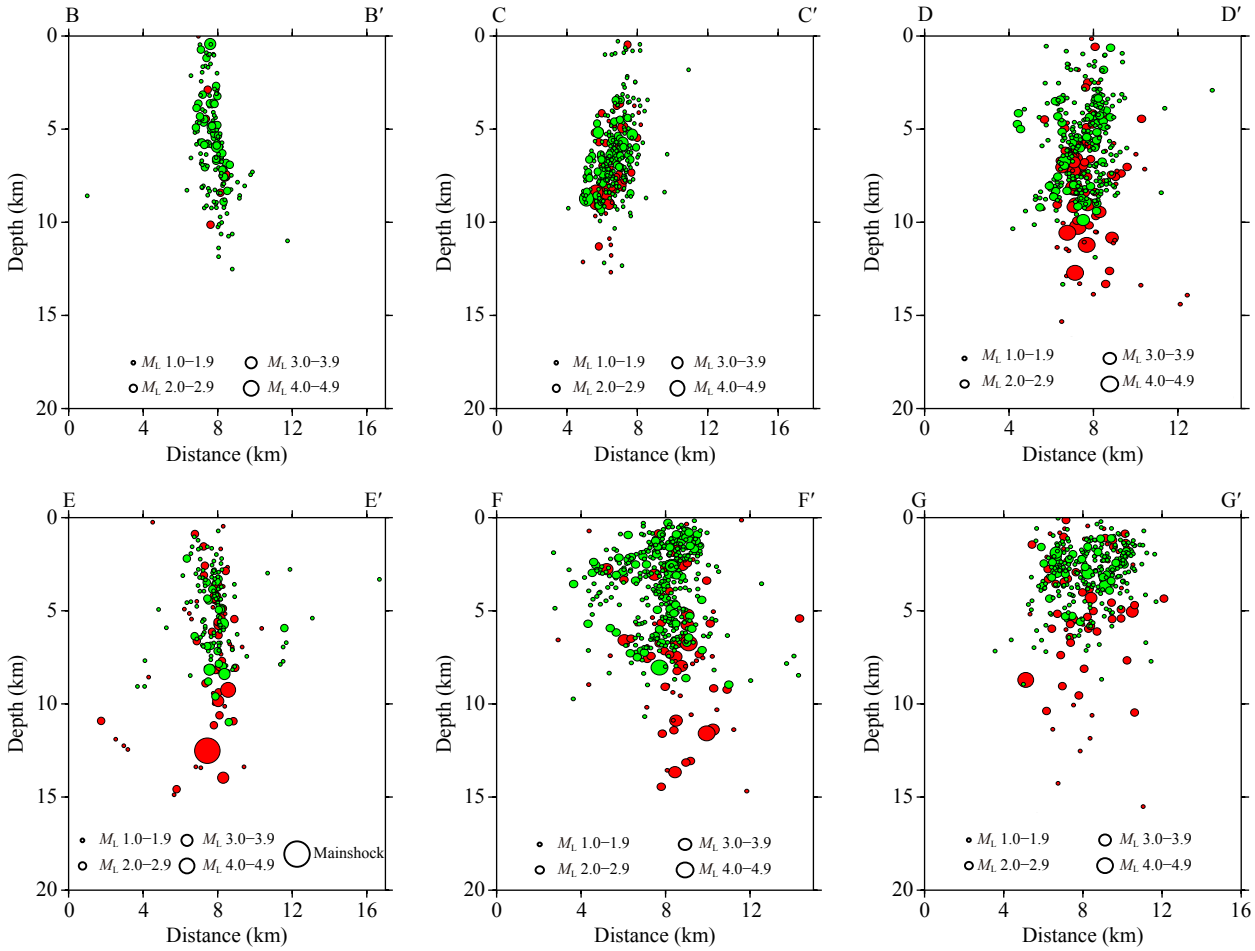

Figure 6. Six vertical cross-sections perpendicular to the strike of the long-axis of the aftershock area. From south to north, there are cross-sections BB', CC', DD', EE', FF', and GG'. Projection width for each side is 2 km for each section.

prove the coverage of aftershocks and the reliability and stability of the data (Table 2). Among the relocated 534 earthquakes in the first three days, 287 occurred before the operation of portable station L6201, and 467 before station L5111; thus, in the first three days, about 87% of the earthquakes are not constrained by near-station data, leading to relatively large focal depth errors in the locations of early events—including the mainshock. Accordingly, we determined that to study the seismogenic fault structure of the Jiuzhaigou earthquake sequence it would be more reasonable to use the distribution of aftershocks occuring longer than three days after the mainshock than to rely on data from the first three days. It has also been shown that the deployment locations of portable stations after an earthquake will directly affect the location accuracy of aftershocks, and further affect determination of the seismogenic structure (Yi GX et al., 2017b); therefore portable stations should be located as close to the observation target as possible.

3. Focal Mechanism Solutions and Centroid Depths of $M_L \geq 3.5$ Earthquakes

The Jiuzhaigou earthquake sequence occurred in the transition zone between the Tibetan Plateau and the Ordos Block where the deformation of crust and lithosphere is quite strong (Shen XZ et al., 2015), and the crust velocity structure varies significantly in the vicinity of the earthquake source (Xie ZJ et al., 2018). In order to ensure the reliability and stability of the calculation result, to calculate the focal mechanism solutions and centroid depths of the $M_L \geq 3.5$ earthquakes in the Jiuzhaigou earthquake sequence we adopted the presently most commonly used CAP waveform inversion method, which is less dependent on the velocity model (Zhao LS and Helmberger, 1994; Zhu LP and Helmberger, 1996; Zheng Y et al., 2009; Long F et al., 2010; Luo Y et al., 2015; Yi GX et al., 2017a, b ; Li YL et al., 2018).

Yi GX et al. (2017a) have used the CAP method and the 1D velocity model (Figure 2) to calculate the focal mechanisms and centroid depths of 14 $M_L \geq 4.0$ earthquakes in the Jiuzhaigou earthquake sequence. In this paper we used the same velocity model, parameter setting, and station-epicenter distance criterion (300 km) to calculate the focal mechanism solutions and centroid depths (h_{CAP}) of $M_L \geq 3.5$ aftershocks that occurred between Aug. 8 and Oct. 31, 2017, and obtained reliable results for the other 18 $M_L \geq 3.5$ events in this sequence; the result is shown in Table 3.

In order to facilitate the following comparison of focal depths and the analysis of deformation characteristics of the seismogenic structure in the aftershock region, the calculation results of 14 M_L

Table 3. Focal mechanism solutions and centroid depths for the 32 $M_L \geq 3.5$ events of the M_S 7.0 Jiuzhaigou earthquake sequence

Event serial number	Occurrence time		Epicenter location		h_{CAP} (km)	Nodal plane 1			Nodal plane 2			*P* axis		*T* axis		*B* axis		Magnitude, M_W	h_{tomoDD} (km)	Areal strain, *As*
	year-month-day	hh:mm:ss	Latitude (°N)	Longitude (°E)		Strike (°)	Dip (°)	Rake (°)	Strike (°)	Dip (°)	Rake (°)	Azimuth (°)	Plunge (°)	Azimuth (°)	Plunge (°)	Azimuth (°)	Plunge (°)			
01*	2017-08-08	21:19:47.4	33.204	103.816	5	156	79	–9	248	81	–169	112	14	22	2	286	76	6.4	12.5	–0.06
02	2017-08-08	23:51:12.5	33.123	103.873	6	254	79	–154	159	62	–12	119	26	24	10	275	62	3.71	8.0	–0.17
03*	2017-08-09	00:35:18.4	33.151	103.842	8	243	83	–154	149	64	–8	109	23	13	13	257	63	3.99	10.3	–0.11
04*	2017-08-09	05:37:15.1	33.120	103.863	7	145	73	0	55	90	163	101	12	8	12	235	73	4.26	8.2	0
05	2017-08-09	05:41:09.0	33.151	103.840	7	158	65	–9	252	82	–155	118	23	23	11	268	63	4.17	9.0	–0.13
06	2017-08-09	06:24:49.6	33.151	103.840	9	245	80	–156	151	66	–11	110	24	16	9	266	64	3.75	9.2	–0.14
07	2017-08-09	06:49:04.3	33.120	103.867	8	138	74	0	48	90	164	94	11	2	11	228	74	3.86	9.0	0
08*	2017-08-09	08:29:04.6	33.283	103.791	10	360	49	75	202	43	107	101	3	205	78	10	11	4.37	11.6	0.96
09*	2017-08-09	09:22:15.3	33.167	103.836	12	335	73	41	231	51	158	98	14	200	41	354	46	4.28	11.2	0.39
10*	2017-08-09	09:32:48.4	33.295	103.732	11	129	25	10	30	86	115	99	36	324	44	208	25	4.12	8.7	0.27
11*	2017-08-09	10:17:03.5	33.155	103.833	8	255	82	–160	162	70	–9	120	20	27	8	276	68	4.75	10.4	–0.1
12	2017-08-09	20:03:05.1	33.159	103.849	12	328	70	44	220	49	153	89	13	192	45	347	42	3.48	9.4	0.48
13	2017-08-10	02:30:51.6	33.155	103.836	5	140	68	–35	245	58	–154	99	40	194	6	292	49	3.58	7.3	–0.4
14*	2017-08-10	03:02:13.6	33.278	103.783	3	155	77	–10	247	80	–167	111	16	21	2	283	74	4.05	6.7	–0.08
15*	2017-08-10	05:05:55.2	33.169	103.823	10	165	78	3	74	87	168	120	6	29	11	241	78	4.65	12.7	0.02
16*	2017-08-10	09:54:02.8	33.165	103.844	6	330	84	21	238	69	174	102	10	196	19	345	68	3.87	8.2	0.08
17	2017-08-10	15:30:10.9	33.150	103.850	8	246	85	–161	154	71	–5	112	17	19	10	260	70	3.73	7.2	–0.06
18	2017-08-10	17:38:31.8	33.278	103.740	9	162	19	60	13	74	100	96	28	298	60	191	9	3.69	2.8	0.92
19*	2017-08-10	17:48:35.0	33.200	103.804	10	340	86	23	248	67	176	112	13	207	19	349	67	4.3	9.3	0.06
20	2017-08-11	08:05:10.5	33.169	103.836	8	331	82	19	238	71	172	103	7	196	19	353	70	3.33	9.1	0.09
21*	2017-08-11	19:26:22.4	33.118	103.858	8	140	75	6	48	84	165	95	6	3	15	208	74	3.91	8.4	0.05
22*	2017-08-12	07:56:39.5	33.121	103.850	8	50	85	166	141	76	5	96	6	5	13	211	75	4.02	8.7	0.04
23*	2017-08-13	22:38:32.7	33.095	103.882	9	145	74	–20	241	71	–163	102	25	193	2	288	65	3.81	7.8	–0.18
24	2017-08-19	19:52:11.8	33.119	103.883	5	261	24	–154	147	80	–68	81	50	219	31	323	21	3.93	5.3	–0.58
25	2017-08-25	04:28:52.0	33.079	103.902	4	147	87	–9	237	81	–177	102	8	193	4	309	81	3.69	4.9	–0.02
26	2017-08-27	08:58:13.7	33.219	103.729	9	149	37	21	42	78	125	105	24	348	46	213	34	3.95	9.3	0.45
27	2017-09-06	01:57:20.8	33.255	103.783	3	156	85	–9	247	81	–175	111	10	202	3	307	80	3.82	2.4	–0.03
28	2017-09-07	12:15:30.4	33.112	103.882	4	140	85	–6	231	84	–175	95	8	185	1	280	82	3.85	5.7	–0.02
29	2017-09-13	07:59:42.5	33.272	103.775	3	254	67	–175	162	85	–23	116	19	210	13	331	66	3.76	2.6	–0.07
30	2017-10-05	03:18:12.5	33.316	103.762	4	264	85	–160	172	70	–5	130	18	36	10	277	69	3.75	3.0	–0.06
31	2017-10-06	18:25:35.3	33.264	103.771	8	334	69	36	229	57	155	99	8	196	40	0	49	4.11	8.0	0.4
32	2017-10-14	11:02:14.9	33.123	103.777	5	248	46	160	352	76	46	113	18	221	42	6	42	3.65	3.1	0.39

*A sterisk after the serial number indicates that the focal mechanism solution and centroid depth h_{CAP} of the earthquake are from Yi G X et al. (2017a); the relocated depth h_{tomoDD} of the event comes from the present study.

≥4.0 earthquakes previously obtained by Yi GX et al. (2017a) are also listed in Table 3 and marked by an asterisk after the event serial number; meanwhile the Table also includes the relocated focal depths of corresponding events denoted as h_{tomoDD}, i.e., the initial rupture depths (Gao Y et al., 1997). Table 3 shows that the source centroid depths h_{CAP} of 32 $M_L \geq 3.5$ events of the Jiuzhaigou earthquake sequence are distributed between 3–12 km with an average depth of 7.25 km—close to the dominant depth range (0–10 km) and average depth 6.7 km of the whole relocated sequence. Except for the Number 1 M_S 7.0 mainshock and Numbers 14 and 18 aftershocks, the differences between h_{CAP} and h_{tomoDD} of the other 29 aftershocks are all within 3 km; the average difference between h_{CAP} and h_{tomoDD} of 31 $M_L \geq 3.5$ aftershocks is 1.53 km.

By analyzing the depth differences between h_{CAP} and h_{tomoDD} in different time intervals in Table 3, we find that for the 15 $M_L \geq 3.5$ aftershocks (No.s 2-16 in Table 3) that took place before the operation of portable station L5111 (see Table 2 for data starting time) the average depth difference is 1.96 km, but for 10 of these aftershocks it is greater than 2 km. Among the 16 $M_L \geq 3.5$ aftershocks (No.s 17–32) that occurred after the operation of station L5111, however, the depth differences of 15 of the 16 events (the sole exception being No.18) are less than 2 km (indeed, of 8 events they are less than 1 km), indicating that the difference is systematically decreased. For these 16 aftershocks occurring more than three days after the mainshock, the average difference between h_{CAP} and h_{tomoDD} is reduced to 1.15 km, significantly lower than for the earlier events. We attribute this difference to data of greater accuracy from the portable stations deployed closer to the aftershock zone three days or more after the mainshock (see Table 2, Figure 2, and Figure 4), indicating that near-station data are vitally important in focal depth determination, and also further indicating that it may be more reasonable to use the spatial distribution of the aftershocks that occurred three days or more after the mainshock for studying the geometric structure of seismogenic fault of the Jiuzhaigou earthquake sequence. The centroid depths h_{CAP} derived from waveform inversion of the later aftershocks are close to the relocated initial rupture depths h_{tomoDD} derived from seismic phase data, indicating that the source centroid depths from waveform inversion and focal depths from aftershock relocation of the later aftershocks in this paper are reliable.

The rose diagrams of nodal plane parameter statistics of 32 $M_L \geq 3.5$ earthquakes of the Jiuzhaigou earthquake sequence (Figure 7) show that the nodal plane strikes are concentrated around two dominant directions of SSE and SWW, the rakes are concentrated around 0° and 180°, displaying typical characteristics of strike slip motion; the dip angles are concentrated between 60° and 90°, indicating a steep fault plane, which is consistent with the result derived from the early part data of the sequence only (Yi GX et al., 2017a). The strike of the SSE nodal plane is consistent with the NNW-trending of the major axes of isoseismic lines and the aftershock zone; the average strike is about 153° and the average dip is about 70°, indicating that the seismogenic fault has an overall strike in the SSE and a steep dip, which tallies with the geometrical characteristic acquired from relocation. Further analysis indicates that, taking the mainshock as the boundary, in the southern part of the aftershock zone the average strike of the SE/SSE nodal planes of the mainshock and 21 aftershocks is about 150° and the average dip angle is about 75°, while in the northern part the average strike of the SE/SSE nodal planes of 10 aftershocks is about 159° and the average dip angle is about 59°, indicating that the southern segment of the fault plane is steeper than the northern segment, and at the same time the strike of the northern segment is deflected northward to some degree.

4. Analysis of the Kinematic and Tectonic Deformation Characteristics of the Seismogenic Faults

In order to analyze straightforwardly the characteristics of the focal mechanism types of the Jiuzhaigou earthquake sequence, and the kinematic and tectonic deformation characteristics of the seismogenic faults, we adopted the rosette method of Amelung and King (1997) and the areal strain value *As* of Vallage et al. (2014) to carry out a further study.

4.1 Classification of Focal Mechanism Solutions of Jiuzhaigou Earthquake Sequence and the Kinematic Characteristics of the Seismogenic Faults

Areal strain *As* is the length difference of the compressional white lobes and extensional black lobes of the strain rosette; the focal mechanism and tectonic deformation classification criteria based on *As* values are as follows: $-1 \leq As < -0.7$, extensional normal faulting; $-0.7 \leq As < -0.3$, oblique extensional normal faulting; $-0.3 \leq As < 0.3$, strike-slip faulting; $0.3 \leq As < 0.7$, oblique compressional thrust faulting; $0.7 \leq As \leq 1$, compressional thrust faulting (Vallage et al., 2014; Yi GX et al., 2016).

The *As* values of 32 $M_L \geq 3.5$ earthquakes derived from the focal mechanism solutions are listed in Table 3; among them the *As* values of two aftershocks (events No.8 and 18 in Table 3) are close to 1, being pure compressional thrusting type, and both occurred in

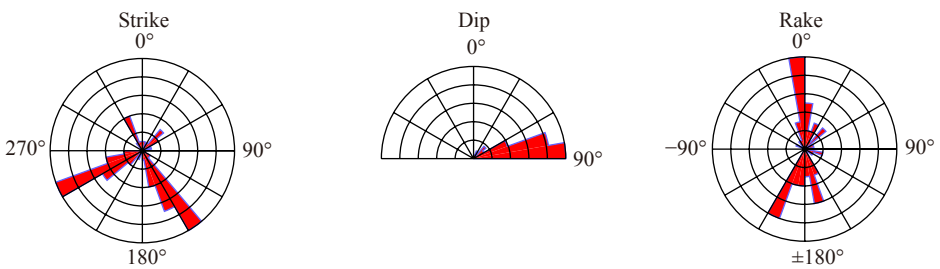

Figure 7. Rose diagrams of the strike, dip, rake of nodal planes for the 32 $M_L \geq 3.5$ events of the M_S 7.0 Jiuzhaigou earthquake sequence.

the northern part of the aftershock zone; the *As* values of two aftershocks (No.s 13 and 24) are between –0.7 and –0.3, being oblique-slip extensional normal fault type, and both occurred in the southern part of the aftershock zone; the *As* values of 5 aftershocks (No.s 9, 12, 26, 31, and 32) are between 0.3 and 0.7, being oblique-slip compressional thrusting type, and occurred on the two sides around the M_S 7.0 mainshock; the *As* values of the mainshock and the rest of the 22 aftershocks are between –0.3 and 0.3, being strike-slip type and counting for about 72% of the total earthquakes, and most are of the pure strike-slip type with *As* values close to 0; the strike-slip earthquakes mainly occurred to the south of the mainshock (Figure 8).

Among the 22 events on the southern segment of the aftershock zone, 18 are strike-slip earthquakes, close to a proportion of 82%; among the 10 earthquakes on the northern segment, however, the proportion of pure compressional thrusting and oblique-slip thrusting events reaches 50%, significantly lowering the proportion of strike-slip events compared to the southern segment, indicating a remarkable difference in the kinematic characteristics of the seismogenic fault between the southern and northern parts of the aftershock zone.

4.2 Analysis of the Tectonic Deformation Characteristics of the Seismogenic Faults

Amelung and King (1997) put forward the strain rosette method to extract horizontal tectonic deformation from focal mechanism solutions, now considered a rather powerful tool for quantitatively comparing the strain mode (Vallage et al., 2014; Yi GX et al., 2016). A strain rosette visualizes the regional tectonic strain mode (Amelung and King, 1997); its major axis of black lobes represents the direction of extension, and that of the white lobes represents compressional direction.

Figure 9 shows the strain rosettes and *P* axis orientations of 32 $M_L \geq$ 3.5 earthquakes of the Jiuzhaigou earthquake sequence, which we use in analyzing the tectonic deformation characteristics of the seismogenic fault. In the lower left of the figure, the strain rosettes and corresponding *As* values of the whole sequence of main event and 31 aftershocks—22 earthquakes on the southern

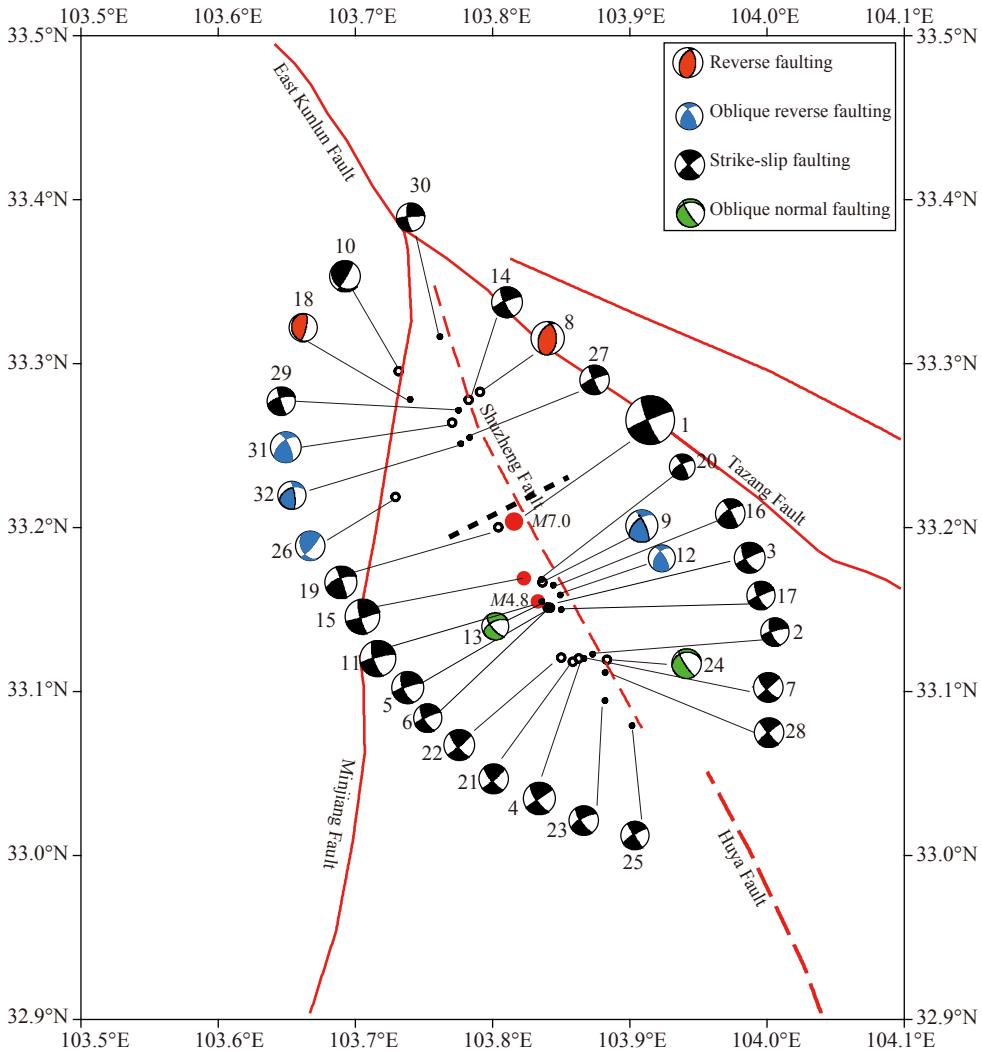

Figure 8. Focal mechanisms of the $M_L \geq 3.5$ earthquakes of the M_S 7.0 Jiuzhaigou earthquake sequence. The number beside each beachball accords with the serial number in the first column of Table 3, and the thick black dashed line divides the aftershock zone into a northern and a southern part.

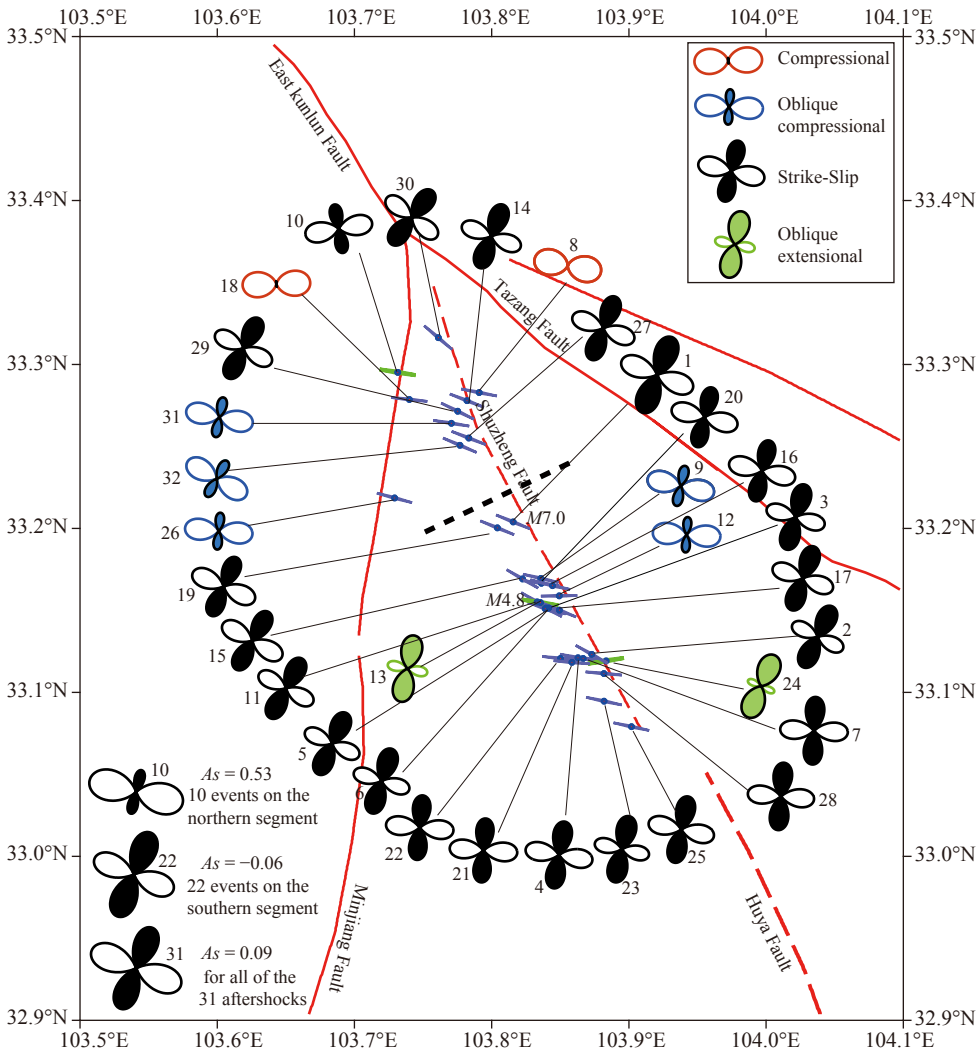

Figure 9. The strain rosettes and *P*-axis orientations of the $M_L \geq 3.5$ Jiuzhaigou earthquake sequence. The short solid lines indicate the *P*-axis orientation; while the blue and green lines show the plunge of *P*-axis < 30° and ≥ 30°, respectively. The black dashed line is the segmentation mark. The strain rosettes for the entire sequence of main event and 31 $M_L \geq 3.5$ aftershocks, 22 $M_L \geq 3.5$ events on the southern segment and 10 $M_L \geq 3.5$ events on the northern segment, are shown in the lower left corner, respectively. The number marked by the side of each strain rosette is the same as in Table 4.

segment and 10 aftershocks on the northern segment—are also shown. The figure demonstrates that all the long axes of compressional white lobes of the rosettes of 32 $M_L \geq 3.5$ earthquakes in this sequence are in the NW-SE/NWW-SEE directions, and the long axes of extensional black lobes are dominantly in the NNE-SSW direction; in the southern part of the aftershock zone most strain rosettes, including that of the mainshock (No.1 in Figure 9), are characterized by nearly equally long white and black lobes, while in the northern part the compressional white lobes of most strain rosettes are obviously larger than their extensional black lobes, indicating that the kinematic and tectonic deformation characteristics in the northern and southern parts of the aftershock zone are different.

The strain rosette for the whole of the 31 $M_L \geq 3.5$ aftershocks accords with that of the M_S 7.0 Jiuzhaigou mainshock (including orientation and shape), indicating that the co-seismic and post-seismic tectonic deformation of the seismogenic fault is the same (Yi GX et al., 2017a); they all exhibit NWW-SEE compression and NNE-SSW extension, the corresponding *As* values being 0.09 and −0.06, respectively, indicating that the lengths of white and black lobes are basically equal, i.e., the amount of compression and extension is approximately the same, which means that both the mainshock and the whole of the aftershocks exhibit nearly pure strike-slip deformation.

However, the calculation results demonstrate that the composite strain rosettes and *As* values of the southern and northern segments of the aftershock zone differ obviously. In the southern segment the composite strain rosette of 22 $M_L \geq 3.5$ earthquakes is consistent with that of the M_S7.0 mainshock, and the areal strain *As* value is −0.06, indicating that the tectonic deformation of the seismogenic fault in that part of the aftershock zone is nearly pure strike-slip, whereas the composite train rosette of 10 $M_L \geq 3.5$ aftershocks in the northern part is obviously different, the extensional black lobes of their strain rosette being much smaller than

the compressional white lobes, and the areal strain *As* value of 0.52 indicating that the seismigenic fault in the northern aftershock zone exhibits oblique compressional deformation with a certain amount of strike component. The above result shows that the tectonic deformation mode of the seismogenic fault of Jiuzhaigou earthquake has obvious segmental characteristic between the north and south. In addition, it is not difficult to observe that the compressional white lobes of the strain rosettes of No.s 10, 18, and 26 aftershocks in the northern aftershock zone are all larger than their extensional black lobes, indicating that the motion mode of the northern segment of the Minjiang Fault is of thrusting with some strike component (Chen SF et al., 1994); the tectonic deformation exhibits an oblique compressional thrusting mode.

The *P* axes of 32 $M_L \geq 3.5$ earthquakes are dominantly near-horizontal in the NWW-SEE direction (see blue and green bars in Figure 9), which tallies with previous study results, including the dominant polarization direction of fast shear waves in the epicenter area (Zhang H et al., 2012; Chang LJ et al., 2008, 2016), the motion velocity field derived from GPS observation (Shi FQ et al., 2018; Zhao DZ et al., 2018), and the regional tectonic stress field direction (Kan RJ et al., 1983). The average azimuth and plunge of *P* axes is 105° and 17°, respectively (Figure 10a); the average plunge of *T* axes is 20°, the dominant azimuth is NNE-SSW (Figure 10b); the average azimuth and plunge of *P* and *T* axes are consistent with the statistic result of focal mechanism solutions in the early stage of the sequence (Yi GX et al., 2017a), indicating that the tectonic stress field in the source region is stable after the mainshock. The above described tectonic stresses with near horizontal NWW-SEE *P* axis and NNE-SSW *T* axis are favorable to the left-lateral strike-slip motion of NNW-SSE-trending faults.

Previous studies have indicated that the orientation of the *P*-axis (Wang XS et al., 2015) and the direction of principal compressional strain (Chen CY et al., 2013; Wu YQ et al., 2015) of the regional tectonic stress field around the epicenter of Jiuzhaigou earthquake all manifest a character of clockwise rotation. This phenomenon is probably caused by the fact that under the persistent northward compression of the Indian Plate the relatively weak material of the Tibetan Plateau is extruded laterally (Tapponnier et al., 1982; Molnar and Lyon-Caent, 1989), and is then blocked by the rigid Ordos Block and the South China Block (Sichuan Basin) on the northeast and southeast respectively, causing the bend in material transfer direction. Such a series of actions probably caused the remarkable difference between the strike-slip movement of the seismogenic fault (Shuzheng Fault) of the M_S 7.0 Jiuzhaigou earthquake (Yi GX et al., 2017a) and the thrusting motion with strike-slip component of the Huya Fault in the south (Zhao XL et al., 1994; Zhou RJ et al., 2000; Zhang YQ et al., 2012), where two *M* 7.2 earthquakes took place at Songpan–Pingwu in 1976 (Kan RJ et al., 1983; Jones et al., 1984) (Figure 1). Therefore, the M_S 7.0 Jiuzhaigou earthquake was caused by the accumulation of long-term tectonic strain energy in the east boundary of the Bayan Har Block at the eastern margin of the Tibetan Plateau, due to the lateral extrusion of crustal material (Yi GX et al., 2017a).

5. Recognition and Conclusion

This paper used seismic data from Aug. 8 to Oct. 31, 2017 provided by the Sichuan Regional Seismological Station Network Center and the tomoDD method to relocate the M_S 7.0 Jiuzhaigou earthquake sequence of Aug. 8, 2017, and analyzed the geometrical characteristics of the seismogenic structure of this earthquake sequence; in the meantime, utilizing the 1D velocity model of the study area and the CAP waveform inversion method we acquired the focal mechanism solutions and centroid depths of the $M_L \geq 3.5$ earthquakes in this sequence; using strain rosettes and areal strain *As* values we further analyzed the kinematic and tectonic deformation characteristics of the seismogenic fault of this earthquake sequence. The resultant major recognitions and conclusions are as follows:

(1) The aftershock sequence of the M_S 7.0 Jiuzhaigou earthquake occurred along the NNW-SSE direction in the area between two branch faults of the eastern terminus of the East Kunlun Fault Belt, i.e., the NW-trending Tazang Fault and the near-NS-trending Minjiang Fault; the aftershock zone is about 38 km long, narrower and deeper in the south and wider and shallower in the north. The relocated mainshock depth is 12.5 km; the dominant aftershock depth range is 0–10 km, with an average depth of 6.7 km. The mainshock epicenter is approximately at the center of the aftershock zone, displaying the character of bilateral rupture. The centroid depths of 32 $M_L \geq 3.5$ earthquakes in the sequence are in the range 3–12 km, with an average depth about 7.3 km, which is basically in accordance with the relocated depth of the sequence.

(2) In the southern aftershock zone south of the mainshock the geometry of the seismogenic fault is relatively simple; the overall strike of the fault is about 150°, the dip angle is about 75°, but the dip direction and dip angle vary to a certain degree in the deep part. In the northern segment of the aftershock zone the seismogenic fault structure is relatively more complex; multiple faults, including the Minjiang Fault, might be involved in the aftershock activity. The overall strike of this fault segment is about 159°, the

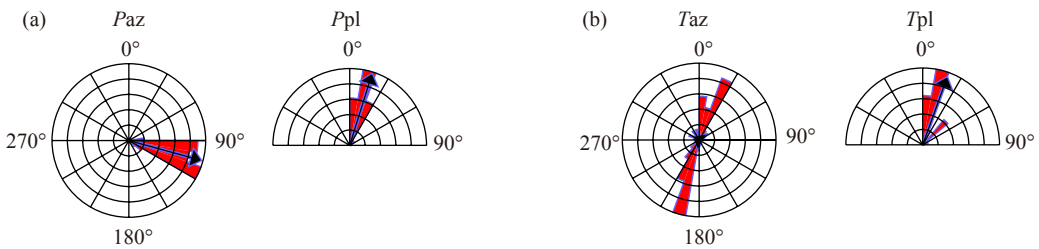

Figure 10. Rose diagrams of the azimuth (az) and plunge (pl) of *P*-axis and *T*-axis of the Jiuzhaigou earthquake sequence.

dip angle is about 59°; compared to the southern segment the fault strike is reflected northward to some degree, and the dip angle is smaller than in the southern segment, indicating that an obvious difference exists in the geometric structure of the seismogenic fault between its southern and northern segments.

(3) The focal mechanism solutions of the 32 $M_L \geq 3.5$ earthquakes in the sequence are dominantly of strike-slip type (about 72% of the total); however the focal mechanism types have obvious segmental characteristics: on the southern segment the strike-slip type is absolutely dominant (almost 82% of the 22 $M_L \geq 3.5$ earthquakes), while on the northern segment 50% of the 10 $M_L \geq 3.5$ earthquakes are of the compressional thrusting and oblique thrusting type, greatly reducing the proportion of strike-slip type compared to those on the southern segment, thus indicating that the kinematic characteristics of the southern and northern fault segments are significantly different.

(4) Both the strain rosette of the M_S 7.0 mainshock and the composite strain rosette of 31 $M_L \geq 3.5$ aftershocks have NWW-SEE compressional white lobes and NNE-SSW extensional black lobes of approximately equal length, the corresponding areal strain *As* values being respectively −0.06 and 0.09, meaning that the deformation of the mainshock and the overall deformation of aftershocks are both nearly pure strike-slip. But the composite strain rosettes and areal strain *As* values of the southern and northern segments are remarkably different; the composite strain rosette and *As* value of the southern segment accord with those of the M_S 7.0 mainshock, indicating the tectonic deformation of the seismogenic fault in the southern aftershock zone is nearly pure strike-slip; the composite strain rosette and *As* value of the northern segment are obviously different, the extensional black lobes of the strain rosette being much smaller than the compressional white lobes and the *As* value being 0.52, indicating that the tectonic deformation of the seismogenic fault in the northern aftershock zone is oblique thrusting with a certain amount of strike-slip component. The above results reveal that the tectonic deformation mode of the seismogenic fault has obvious segmental characteristics between its south and north.

(5) 87% of the earthquakes occurring in the first three days lack near-station constraints, so their depth errors are relatively large. To study the geometric structure of the seismogenic fault of the Jiuzhaigou earthquake sequence we have found it more reasonable to use the aftershocks three days or more after the mainshock. Our analysis demonstrates that the deployment locations of portable stations after the mainshock directly affect the location accuracy of aftershocks and the identification of seismogenic fault. This study provides additional evidence that the locations of portable stations should be as close to the observation target as possible.

Acknowledgments

We are grateful to Prof. Zhu Lupei of San Luis University of the United States for providing the CAP program, to Prof. Yann Klinger and Dr. Amaury Vallage of Paris Institute of Geophysics, France, for providing the strain rosette program, and to the reviewers for valuable suggestions. GMT software was used to plot a part of the figures. The research was supported by National Science Foundation of China (41574047) and National Key R & D Program of China (2018YFC150330501).

References

Aki, K. (1984). Asperities, barriers, characteristic earthquakes and strong motion prediction. *J. Geophys. Res. Solid Earth*, *89*(B7), 5867–5872. https://doi.org/10.1029/JB089iB07p05867

Amelung, F., and King, G. (1997). Large-scale tectonic deformation inferred from small earthquakes. *Nature*, *386*(6626), 702–705. https://doi.org/10.1038/386702a0

An, Y. R., Su, J. R., Xue, Y., Zhang, Y. Y., Bai, L. S., Liu, J., He, S. L., Yang, Z. G., Du, G. B., Wei, Y. L., Wu, W. W., Huang, C. M., and Pan, Y. (2018). Seismologic characteristics of the 2017, M_S 7.0 Jiuzhaigou earthquake, Sichuan, China. *Chinese Sci. Bull.* (*in Chinese*), *63*(7), 663–673. https://doi.org/10.1360/N972017-00919

Chang, L. J., Wang, C. Y., and Ding, Z. F. (2008). Seismic anisotropy of upper mantle in Sichuan and adjacent regions. *Sci. China Ser. D Earth Sci.*, *51*(12), 1683–1693. https://doi.org/10.1007/s11430-008-0147-8

Chang, L. J., Ding, Z. F., and Wang, C. Y. (2016). Upper mantle anisotropy beneath the northern segment of the north-south tectonic belt in China. *Chinese J. Geophys.* (*in Chinese*), *59*(11), 4035–4047. https://doi.org/10.6038/cjg20161109

Chen, C. Y., Ren, J. W., Meng, G. J., Yang, P. X., Xiong, R. W., Hu, C. Z., Su, X. N., and Su, J. F. (2013). Division, deformation and tectonic implication of active blocks in the eastern segment of Bayan Har block. *Chinese J. Geophys.* (*in Chinese*), *56*(12), 4125–4141. https://doi.org/10.6038/cjg20131217

Chen, S. F., Wilson, C. J. L., Deng Q. Q., Zhao, X. L., and Zhi, L. L. (1994). Active faulting and block movement associated with large earthquakes in the Min Shan and Longmen Mountains, northeastern Tibetan Plateau. *J. Geophys. Res. Solid Earth*, *99*(B12), 24025–24038. https://doi.org/10.1029/94JB02132

Chen, W., Qiao, X. J., Liu, G., Xiong, W., Jia, Z. G., Li, Y., Wang, Y. B., You, X. Z., and Long F. (2018). Study on the coseismic slip model and Coulomb stress of the 2017 Jiuzhaigou M_S 7.0 earthquake constrained by GNSS and inSAR measurements. *Chinese J. Geophys.* (*in Chinese*), *61*(5), 2122–2132. https://doi.org/10.6038/cjg2018L0613

Fang, L. H., Wu, J. P., Su, J. R., Wang, M. M., Jiang, C., Fan, L. P., Wang, W. L., Wang, C. Z., and Tan, X. L. (2018). Relocation of mainshock and aftershock sequence of the M_S 7.0 Sichuan Jiuzhaigou earthquake. *Chinese Sci. Bull.* (*in Chinese*), *63*(7), 649–662. https://doi.org/10.1360/N972017-01184

Gao, Y., Zhou, H. L., Zheng, S. H., Ma, L., Che, S., and Liu, W. H. (1997). Preliminary discussion on implication of determination on source depth of earthquake. *Earthq. Res. China* (*in Chinese*), *13*(4), 321–329.

Gomberg, J. S., Shedlock, K. M., and Roecker, S. W. (1990). The effect of S-wave arrival times on the accuracy of hypocenter estimation. *Bull. Seismol. Soc. Amer.*, *80*(6A), 1605–1628.

Han, L. B., Cheng, J., An, Y. R., Fang, L. H., Jiang, C. S., Chen, B., Wu, Z. L., Liu, J., Xu, X. W., Liu, R. F., Yao, Z. X., Wang, C. Z., and Wang, Y. S. (2018). Preliminary report on the 8 August 2017 M_S 7.0 Jiuzhaigou, Sichuan, China, earthquake. *Seismol. Res. Lett.*, *89*(2A), 557–569. https://doi.org/10.1785/0220170158

Ji, L. Y., Liu, C. J., Xu, J., Liu, L., Long, F., and Zhang, Z. W. (2017). InSAR observation and inversion of the seismogenic fault for the 2017 Jiuzhaigou M_S 7.0 earthquake in China. *Chinese J. Geophys.* (*in Chinese*), *60*(10), 4069–4082. https://doi.org/10.6038/cjg20171032

Jones, L. M., Han, W. B., Haukkson, E., Jin, A. S., Zhang, Y. G., and Luo, Z. L. (1984). Focal mechanisms and aftershock locations of the Songpan earthquakes of August 1976 in Sichuan, China. *J. Geophys. Res. Solid Earth*, *89*(B9), 7697–7071. https://doi.org/10.1029/JB089iB09p07697

Kan, R. J., Wang, S. J., Huang, K., and Song, W. (1983). Modern tectonic stress field and relative motion of intraplate block in southwestern China. *Seismol. Geol.* (*in Chinese*), *5*(2), 79–90.

Kato, A., Miyatake, T., and Hirata, N. (2010). Asperity and barriers of the 2004 Mid-Niigata Prefecture earthquake revealed by highly dense seismic observations. *Bull. Seismol. Soc. Amer*, *100*(1), 298–306.

https://doi.org/10.1785/0120090218

Li, M. J., Shen, X. Z., Zhang, Y. S., Liu, X. Z., and Mei, X. P. (2018). Fine crustal structures of northeast margin of the Tibetan Plateau and structural features of Jiuzhaigou earthquake focal area constrained by the data from a high-density seismic array. *Chinese J. Geophys.* (*in Chinese*), *61*(5), 2075–2087. https://doi.org/10.6038/cjg2018L0720

Li, Y. L., Wang, B. S., He, R. Z., Zheng, H. W., Yan, J. Y., and Li Y. (2018). Fine relocation, mechanism, and tectonic indications of middle-small earthquakes in the Central Tibetan Plateau. *Earth Planet. Phys.*, *2*(5), 406–419. https://doi.org/10.26464/epp2018038

Liang, J. H., Sun, L., and Liu, J. (2018). A high precision relocation study of the M_S 7.0 Jiuzhaigou earthquake and the aftershocks occurred in 2017. *Chinese. J. Geophys.* (*in Chinese*), *61*(5), 2152–2162. https://doi.org/10.6038/cjg2018L0604

Liang, S. S., Lei, J. S., Xu, Z. G., Xu, X. W., Zou, L. Y., Liu, J. G., and Chen, H. F. (2018). Relocation of aftershocks of the 2017 Jiuzhaigou, Sichuan, M_S 7.0 earthquake and inversion for focal mechanism of the mainshock. *Chinese J. Geophys.* (*in Chinese*), *61*(5), 2163–2175. https://doi.org/10.6038/cjg2018L0508

Long, F., Zhang, Y. J., Wen, X. Z., Ni, S. D., and Zhang, Z. W. (2010). Focal mechanism solutions of $M_L \geq 4.0$ events in the M_S 6.1 Panzhihua-Huili earthquake sequence of Aug 30:2008. *Chinese J. Geophys.* (*in Chinese*), *53*(12), 2852–2860. https://doi.org/10.3969/j.issn.0001-5733.2010.12.008

Luo, Y., Zhao, L., Zeng, X. F., and Gao, Y. (2015). Focal mechanisms of the Lushan earthquake sequence and spatial variation of the stress field. *Sci. China Earth Sci.*, *58*(7), 1148–1158. https://doi.org/10.1007/s11430-014-5017-y

Lu, R. Q., Xu, X.W., Chen, L. C., Chen, G. H., Yao, Q., Sun, J. B., Ren, J. J., Ren, Z. K., Xu, C., Wei, Z. Y., Tan, X. B., Dong, S. P., Shi, F., and Wu, X. Y. (2018). Seismotectonics of the 8 August 2017 Jiuzhaigou earthquake and the three-dimensional fault models in the seismic region. *Seismology and Geology* (*in Chinese*), *40*(1), 1–11. https://doi.org/10.3969/j.issn.0253-4967.2018.01.001

Molnar, P., and Lyon-Caent, H. (1989). Fault plane solutions of earthquakes and active tectonics of the Tibetan Plateau and its margins. *Geophys. J. Int.*, *99*(1), 123–153. https://doi.org/10.1111/gji.1989.99.issue-1

Qi, Y. P., Long, F., Xiao, B. F., Lu, Q., and Jiang, P. (2018). Focal mechanism solutions and tectonic stress field characteristics of the 2017 M_S 7.0 Jiuzhaigou earthquake sequence. *Acta Geosci. Sin.* (*in Chinese*), *39*(5), 622–634. https://doi.org/10.3975/cagsb.2018.061901

Rubin, A. M. (2002). Aftershocks of microearthquakes as probes of the mechanics of rupture. *J. Geophys. Res. Solid Earth*, *107*(B7), 2142. https://doi.org/10.1029/2001JB000496

Shan, B., Zheng, Y., Liu, C. L., Xie, Z. J., and Kong, J. (2017). Coseismic Coulomb failure stress changes caused by the 2017 *M* 7.0 Jiuzhaigou earthquake, and its relationship with the 2008 Wenchuan earthquake. *Sci. China Earth Sci.*, *60*(12), 2181–2189. https://doi.org/10.1007/s11430-017-9125-2

Shan, X. J., Qu, C. Y., Gong, W. Y., Zhao, D. Z., Zhang, Y. F., Zhang, G. H., Song, X. G., Liu, Y. H., and Zhang, G. F. (2017). Coseismic deformation field of the Jiuzhaigou M_S 7.0 earthquake from Sentinel-1A InSAR data and fault slip inversion. *Chinese J. Geophys.* (*in Chinese*), *60*(12), 4527–4536. https://doi.org/10.6038/cjg20171201

Shen, X. Z., Yuan, X. H., and Liu, M. (2015). Is the Asian lithosphere underthrusting beneath northeastern Tibetan Plateau? Insights from seismic receiver functions. *Earth Planet. Sci. Lett.*, *428*, 172–180. https://doi.org/10.1016/j.epsl.2015.07.041

Shi, F. Q., Shao, Z. G., Zhan, W., Ding, X. G., Zhu, L., and Li, Y. J. (2018). Numerical modeling of the shear modulus and stress state of active faults in the northeastern margin of the Tibetan Plateau. *Chinese J. Geophys.* (*in Chinese*), *61*(9), 3651–3663. https://doi.org/10.6038/cjg2018L0631

Sun, J. B., Yue, H., Shen, Z. K., Fang, L. H., Zhan, Y., and Sun, X. Y. (2018). The 2017 Jiuzhaigou earthquake: A complicated event occurred in a young fault system. *Geophys. Res. Lett.*, *45*(5), 2230–2240. https://doi.org/10.1002/2017GL076421

Tapponnier, P., Peltzer, G., Le Dain, A. Y., Armijo, R., and Cobbold, P. (1982). Propagating extrusion tectonics in Asia: New insights from simple experiments with plasticine. *Geology.*, *10*(12), 611–616. https://doi.org/10.1130/0091-7613(1982)10<611:PETIAN>2.0.CO;2

Vallage, A., Devès, M. H., Klinger, Y., King, G. C. P., and Ruppert, N. A. (2014). Localized slip and distributed deformation in oblique settings: the example of the Denali fault system, Alaska. *Geophys. J. Int.*, *197*(3), 1284–1298. https://doi.org/10.1093/gji/ggu100

Waldhauser, F., and Ellsworth, W. L. (2000). A double-difference earthquake location algorithm: Method and application to the northern Hayward fault, California. *Bull. Seismol. Soc. Amer*, *90*(6), 1353–1368. https://doi.org/10.1785/0120000006

Wang, X. S., Lv, J., Xie, Z. J., Long, F., Zhao, X. Y., and Zheng, Y. (2015). Focal mechanisms and tectonic stress field in the North-South Seismic Belt of China. *Chinese J. Geophys.* (*in Chinese*), *58*(11), 4149–4162. https://doi.org/10.6038/cjg20151122

Wang, Y. B., Gan, W. J., Chen, W. T., You, X. Z., and Lian, W. P. (2018). Coseismic displacements of the 2017 Jiuzhaigou *M* 7.0 earthquake observed by GNSS: Preliminary results. *Chinese J. Geophys.* (*in Chinese*), *61*(1), 161–170. https://doi.org/10.6038/cjg2018L0611

Wen, X. Z. (2018). The 2008 Wenchuan, 2013 Lushan and 2017 Jiuzhaigou earthquakes, Sichuan, in the last more than one thousand years of rupture history of the eastern margin of the Bayan Har block. *Acta Seismol. Sin.* (*in Chinese*), *40*(3), 255–267. https://doi.org/10.11939/jass.20170211

Wu, Y. Q., Jiang, Z. S., Zhao, J., Liu, X. X., Wei, W. X., Liu, Q., Li, Q., Zou, Z. Y., and Zhang, L. (2015). Crustal deformation before the 2008 Wenchuan M_S 8.0 earthquake studied using GPS data. *J. Geodyn.*, *85*, 11–23. https://doi.org/10.1016/j.jog.2014.12.002

Xie, Z. J., Zheng, Y., Yao, H. J., Fang, L. H., Zhang, Y., Liu, C. L., Wang, M. M., Shan, B., Zhang, H. P., Ren, J. J., Ji, L. Y., and Song, M. Q. (2018). Preliminary analysis on the source properties and seismogenic structure of the 2017 Ms7.0 Jiuzhaigou earthquake. *Sci. China Earth Sci.*, *61*(3), 339–352. https://doi.org/10.1007/s11430-017-9161-y

Xu, L. S., Zhang, X., and Li, C. L. (2018). Which velocity model is more suitable for the 2017M_S 7.0 Jiuzhaigou earthquake?. *Earth Planet. Phys.*, *2*, 163–169. https://doi.org/10.26464/epp2018016

Xu, X. W., Chen, G. H., Wang Q. X., Chen L. C., Ren Z. K., Xu, C., Wei, Z. Y., Lu, R. Q., Tan, X. W., Dong, S. P., and Shi, F. (2017). Discussion on seismogenic structure of Jiuzhaigou earthquake and its implication for current strain state in the southeastern Qinghai-Tibet Plateau. *Chinese J. Geophys.* (*in Chinese*), *60*(10), 4018–4026. https://doi.org/10.6038/cjg20171028

Yang, Y., and Chang, L. J. (2018). Variations of shear wave splitting in the source region of the 2017 Jiuzhaigou M_S 7.0 earthquake. *Chinese J. Geophys.* (*in Chinese*), *61*(5), 2088–2098. https://doi.org/10.6038/cjg2018M0174

Yi, G. X., Long, F., Wen, X. Z., Liang, M. J., and Wang, S. W. (2015). Seismogenic structure of the *M* 6.3 Kangding earthquake sequence on 22 Nov. 2014, Southwestern China. *Chinese J. Geophys.* (*in Chinese*), *58*(4), 1205–1219. https://doi.org/10.6038/cjg20150410

Yi, G. X., Long, F., Vallage, A., Klinger, Y., Liang, M. J., and Wang, S. W. (2016). Focal mechanism and tectonic deformation in the seismogenic area of the 2013 Lushan earthquake sequence, southwestern China. *Chinese J. Geophys.* (*in Chinese*), *59*(10), 3711–3731. https://doi.org/10.6038/cjg20161017

Yi, G. X., Long, F., Liang, M. J., Zhang, H. P., Zhao, M., Ye, Y. Q., Zhang, Z. W., Qi, Y. P., Wang, S. W., Gong, Y., Qiao, H. Z., Wang, Z., Qiu, G. L., and Su, J. R. (2017a). Focal mechanism solutions and seismogenic structure of the 8 August 2017 *M* 7.0 Jiuzhaigou earthquake and its aftershocks, northern Sichuan. *Chinese J. Geophys.* (*in Chinese*), *60*(10), 4083–4097. https://doi.org/10.6038/cjg20171033

Yi, G. X., Long, F., Liang, M. J., Zhang, Z. W., Zhao, M., Qi, Y. P., Gong, Y., Qiao, H. Z., Wang, Z., Wang, S. W., and Shuai, L. R. (2017b). Seismogenic structure of the *M* 4.9 and *M* 5.1 Litang earthquakes on 23 September 2016 in southwestern China. *Seismol. Geol.* (*in Chinese*), *39*(5), 949–963. https://doi.org/10.3969/j.issn.0253-4967.2017.05.006

Zhang, H., Gao, Y., Shi, Y. T., Liu, X. F., and Wang, Y. X. (2012). Tectonic stress analysis based on the crustal seismic anisotropy in the northeastern margin of Tibetan plateau. *Chinese J. Geophys.* (*in Chinese*), *55*(1), 95–104. https://doi.org/10.6038/j.issn.0001-5733.2012.01.009

Zhang, H. J., and Thurber, C. H. (2003). Double-difference tomography: the

method and its application to the Hayward fault, California. *Bull. Seismol. Soc. Amer.*, *93*(5), 1875–1889. https://doi.org/10.1785/0120020190

Zhang, H. J., and Thurber, C. (2006). Development and applications of double-difference seismic tomography. *Pure Appl. Geophys.*, *163*(2-3), 373–403. https://doi.org/10.1007/s00024-005-0021-y

Zhang, X., Feng, W. P., Xu, L. S., and Li, C. L. (2017). The source-process inversion and the intensity estimation of the 2017 M_S 7.0 Jiuzhaigou earthquake. *Chinese J. Geophys.* (*in Chinese*), *60*(10), 4105–4116. https://doi.org/10.6038/cjg20171035

Zhang, Y. Q., Li, H. L., Wu, M. L., and Liao, C. T. (2012). Late Cenozoic thrust and Nappe structure along the Minjiang upstream: Evidence from a drill hole. *Geol. Rev.* (*in Chinese*), *58*(2), 215–223. https://doi.org/10.3969/j.issn.0371-5736.2012.02.003

Zhao, B., Gao, Y., and Ma, Y. L. (2018a). Using surface wave amplitude spectra to estimate the source depth of Sichuan Jiuzhaigou *M* 7.0 earthquake. *Chinese Sci. Bull.* (*in Chinese*), *63*(13), 1223–1234. https://doi.org/10.1360/N972017-01150

Zhao, B., Gao, Y., Liang, J. H., and Liu, J. (2018b). Interferometric source estimation of Sichuan Jiuzhaigou M_S 7.0 earthquake. . *Chinese J. Geophys.* (*in Chinese*), *61*(6), 2292–2300. https://doi.org/10.6038/cjg2018L0599

Zhao, D. Z., Qu, C. Y., Shan, X. J., Gong, W. Y., Zhang, Y. F., and Zhang, G. H. (2018). InSAR and GPS derived coseismic deformation and fault model of the 2017 M_S 7.0 Jiuzhaigou earthquake in the Northeast Bayanhar block. *Tectonophysics*, *726*, 86–99. https://doi.org/10.1016/j.tecto.2018.01.026

Zhao, L. S., and Helmberger, D. V. (1994). Source estimation from broadband regional seismograms. *Bull. Seismol. Soc. Amer.*, *84*(1), 91–104.

Zhao, X. L., Deng, Q. D., and Chen, S. F. (1994). Tectonic geomorphology of the Minshan uplift in western Sichuan, southwestern China. *Seismol. Geol.* (*in Chinese*), *16*(4), 429–439.

Zheng, X. J., Zhang, Y., and Wang, R. J. (2017). Estimating the rupture process of the 8 August 2017 Jiuzhaigou earthquake by inverting strong-motion data with IDS method. *Chinese J. Geophys.* (*in Chinese*) , *60*(11), 4421–4430. https://doi.org/10.6038/cjg20171128

Zheng, Y., Ma, H. S., Lü, J., Ni, S. D., Li, Y. C., and Wei, S. J. (2009). Source mechanism of strong aftershocks ($M_S \geq 5.6$) of the 2008/05/12 Wenchuan earthquake and the implication for seismotectonics. *Sci. China Ser. D Earth Sci.*, *52*(6), 739–753. https://doi.org/10.1007/s11430-009-0074-3

Zhou, R. J., Pu, X. H., He, Y. L., Li, X. G., and Ge, T. Y. (2000). Recent activity of Minjiang fault zone, uplift of Minshan block and their relationship with seismicity of Sichuan. *Seismol. Geol.* (*in Chinese*), *22*(3), 285–294. https://doi.org/10.3969/j.issn.0253-4967.2000.03.009

Zhu, L. P., and Helmberger, D. V. (1996). Advancement in source estimation techniques using broadband regional seismograms. *Bull. Seismol. Soc. Amer.*, *86*(5), 1634–1641.